

Solution strategies for two- and three-dimensional electromagnetic inverse problems

Gregory A Newman[†] and G Michael Hoversten[‡]

[†] Sandia National Laboratories, PO Box 5800, Albuquerque, NM 87185-0750, USA

[‡] Lawrence Berkeley National Laboratory, Berkeley, CA 94729, USA

Received 31 January 2000

Abstract. We analyse a variety of solution strategies for nonlinear two-dimensional (2D) and three-dimensional (3D) electromagnetic (EM) inverse problems. To impose a realistic parameterization on the problem, the finite-difference equations arising from Maxwell equations are employed in the forward problem. Krylov subspace methods are then used to solve the resulting linear systems. Because of the efficiencies of the Krylov methods, they are used as the computational kernel for solving 2D and 3D inverse problems, where multiple solutions of the forward problem are required. We derive relations for computing the full Hessian matrix and functional gradient that are needed for computing the model update, via the Newton iteration. Different strategies are then discussed for economically carrying out the Newton iteration for 2D and 3D problems, including the incorporation of constraints necessary to stabilize the inversion process. Two case histories utilizing EM inversion are presented. These include inversion of cross-well data for monitoring electrical conductivity changes arising from an enhanced oil recovery project and the usefulness of cross-well EM methods to characterize the transport pathways for contaminants in the subsurface.

1. Introduction

Within the last decade significant progress has been made in solving 2D and 3D electromagnetic (EM) inverse problems for geophysical applications. Knowledge of the subsurface electrical conductivity, estimated through the inversion process, is critical. It can be utilized in hydrological modelling, mineral, oil and gas exploration, and more recently in reservoir and environmental characterization. Because of large computational demands, solutions have been proposed that utilize approximate forward-modelling methods and data sensitivities (Zhdanov and Fang 1999, Farquharson and Oldenburg 1996, Torres-Verdin and Habashy 1994). Many of these approximate methods rely on the Born approximation or some modified form of it. While these approaches have had some success, they limit themselves to situations where the EM response can be accurately simulated over a limited range of conductivity variation, frequencies and model complexity. For example, it is now understood that these solutions may not be that good for situations where there is a large mutual interaction/coupling in the fields arising from multiple conductors. Because of these limitations it was realized that solutions that simulate the full physics of EM wave propagation and scattering were also required. These latter types of solutions sacrificed speed for accuracy; however, they offer a means to validate the range of applicability of the faster approximate solutions, and provide accurate solutions over the widest range of possible scenarios.

For 2D problems, Newman (1995) demonstrated that approximate solutions to the forward problem could be avoided and it was possible to impose a realistic parametrization on the

problem, thereby producing images of the subsurface that are not underparametrized and undersampled. A full solution to the forward problem was not prohibitive as previously believed, and it could be used as the computational kernel for solving the 2D inverse problem. For 3D problems, Newman and Alumbaugh (1997) avoided direct solution of the normal equations by using conjugate gradients (CGs) to compute the model update; this was the same approach used by Mackie and Madden (1993) for the 3D magnetotelluric inverse problem. With this method all that is required is the ability to efficiently compute a matrix–vector product arising from the normal equations. The 3D problem was also solved on a massively parallel computational platform because of its size and scale; solution times on scalar machines were not practical due to excessive computation times and memory requirements. In the solution of either the 2D or 3D inverse problem, the 3D Maxwell equations were precisely solved using staggered finite differences and highly efficient Krylov subspace methods. It is now recognized that incorporation of these strategies into the inversion algorithms was essential in producing robust and accurate solutions to 2D and 3D EM inverse problems. Because of the inherent accuracy of these types of solutions they could also be used for validating the approximate inversion schemes.

In this paper we revisit and expand upon the computational strategies of Newman (1995) and Newman and Alumbaugh (1997) for solving 2D and 3D EM inverse problems. The formulation that we present reflects a more general and mature treatment of these problems. Using a partial differential equation framework of Maxwell equations, we derive relations for computing the full Hessian matrix and functional gradient that are needed for computing the model update, via the Newton iteration. We also provide different strategies for economically carrying out the Newton iteration for 2D and 3D problems, including the incorporation of constraints necessary to stabilize the inversion process. Essential to these strategies is the ability to efficiently solve the forward problem. Thus we will review the formulation of the forward problem and methods for its solution along with related computational issues. We conclude the paper with two case histories. In the first example, we demonstrate the usefulness of cross-well EM methods to characterize the transport pathways of contaminants in the subsurface. In the second example, cross-well data are inverted for monitoring conductivity changes arising from an enhanced oil recovery project.

2. Formulation of the forward problem

An important consideration in solving the 3D/2D EM inverse problem is that the forward-modelling solution must be able to correctly simulate the responses arising from realistic 3D and 2D geology. Parametrizations of the earth's electrical conductivity on the order of 10^5 to 10^6 are typically required for these types of numerical simulations. Finite-difference modelling techniques, as already mentioned, are very efficient for the task and are employed here. We remark that we also use the 3D solution presented below to simulate responses arising from 2D problems, where the conductivity is invariant along a geological strike. While it is possible to solve such 2D problems quickly by Fourier transforming out the strike direction of the problem (Stoyer and Greenfield 1976), the 3D solution presented below is fast enough so we can also simulate 2D responses with high efficiency.

Assuming a harmonic time dependence of $e^{i\omega t}$ where $i = \sqrt{-1}$ and ω is the angular frequency, and neglecting displacement currents, the electric field, \mathbf{E} , satisfies the vector equation

$$\nabla \times \nabla \times \mathbf{E} + i\omega\mu_0\sigma\mathbf{E} = \mathbf{J}. \quad (1)$$

In this expression the electrical conductivity and magnetic permeability of free space are

denoted by σ and μ_0 respectively; note that σ can be considered to be a complex quantity that varies pointwise in three dimensions. Thus, induced polarization effects can be studied with equation (1). While EM methods can also be sensitive to magnetic permeability changes in the earth, usually such changes are rare in occurrence, except for magnetic ore bodies and a small number of soils that exhibit high magnetic losses. Hence, the assumption that the earth is nonmagnetic in equation (1) is quite reasonable. Dirichlet boundary conditions are applied to equation (1), where the tangential electric-field boundary values are specified to be zero on the boundary of a large box, which fully contains the investigation domain, including the air and earth, as well as sources and receivers. Specification of the source vector \mathbf{J} will depend on whether a total or scattered electric field solution is desired. A scattered-field formulation is usually preferred because the mesh need not be as fine as with a total field solution, and can deliver accuracy to within one per cent, which is typically needed for inverting field data. In a scattered field formulation, we set $\mathbf{E} = \mathbf{E}^s$ in equation (1), and following Newman and Alumbaugh (1995) set

$$\mathbf{J} = i\omega\mu_0\{(\sigma - \sigma_0)\}E^b, \quad (2)$$

where σ_0 defines the background conductivity of uniform media and E^b is the background electric field.

When equation (1) is approximated with finite differences using a Yee (1966) staggered grid and symmetrically scaled (Alumbaugh *et al* 1996, Newman and Alumbaugh 1995), a linear system results:

$$\mathbf{K}\mathbf{E} = \mathbf{S}. \quad (3)$$

The matrix \mathbf{K} is complex-symmetric, depends upon frequency and is sparse with 13 nonzero entries per row. \mathbf{S} is the source vector that depends on the boundary conditions, source-field polarization and frequency of excitation. This system is efficiently solved for each source and frequency using the quasi-minimum residual (QMR) method, which belongs to the class of Krylov subspace techniques that are highly efficient in iteratively solving sparse linear systems. The reader is referred to Alumbaugh *et al* (1996) and Newman and Alumbaugh (1995) for the details of how these techniques are implemented. Once the electric fields have been determined on the mesh, the magnetic fields, \mathbf{H} , can be determined from Faraday's law,

$$\mathbf{H} = \nabla \times \mathbf{E} / -i\omega\mu_0, \quad (4)$$

by numerically approximating the curl of the electric field at various nodal points. One can then interpolate either the electric or magnetic field nodal values to the point of interest.

Even with the benefits of a staggered grid, which implicitly enforces the divergence-free condition on the current density (Smith 1996a), it is sometimes necessary to explicitly enforce this condition, where

$$\nabla \cdot \sigma \mathbf{E} = 0. \quad (5)$$

This can be accomplished in several ways in the numerical solution as frequencies approach the static limit, either through preconditioning (Newman 1999) or with a static-divergence correction procedure (Smith 1996b, Newman and Alumbaugh 1996). Such methods can drastically reduce the time needed to solve equation (3). For cross-well simulations, however, these techniques are not that effective, due in part to higher frequencies employed in the measurements. For more information on the effectiveness and applicability of these solution acceleration techniques, we refer the reader to the above-mentioned references.

3. Formulation of the nonlinear inverse problem

3.1. Regularized least squares

We assume that through a linear complex forward mapping operator, $f[\mathbf{m}]$, we have the ability to compute discrete solutions of Maxwell equations for a real and arbitrary 3D electrical conductivity distribution, \mathbf{m} , within the earth for some source–receiver set combination as shown in figure 1. In many inverse problems the assumption that the conductivity is strictly real is quite reasonable and it avoids additional complications. Techniques for constructing this operator, $f[\mathbf{m}]$, are given below. Thus the observations can be viewed as a function of the model:

$$d^{\text{obs}} = f[\mathbf{m}] + \varepsilon \quad (6)$$

where d^{obs} and ε are complex vectors of length n that comprise the observed data values and measurement noise. The mapping $f[\mathbf{m}]$ takes the real m -dimensional vector, \mathbf{m} and maps it into the complex data space of dimension n . Since the data are noisy and the inverse problem is underdetermined (there are far more model parameters than data points) the process of recovering the model, \mathbf{m} , is unstable and ill-posed; this is the case even in the absence of noise. Thus there is no unique conductivity model that satisfies the data. Hence the process of regularization is used to recover a relatively smooth solution which is unique at least in a localized region of the model space. A technique often used to accomplish this task is to minimize the Tikhonov functional (Tikhonov and Arsenin 1977)

$$\phi = \frac{1}{2} \{ (F[\mathbf{m}] - d^{\text{obs}}) \}^H \{ (F[\mathbf{m}] - d^{\text{obs}}) \} + \frac{\lambda}{2} \| \mathbf{W}(\mathbf{m} - \mathbf{m}_{\text{ref}}) \|^2 \quad (7)$$

where H denotes the Hermitian operator. \mathbf{W} is a real smoothing matrix, which does not depend on \mathbf{m} . There is a variety of choices available for \mathbf{W} . Here \mathbf{W} is based upon a finite-difference

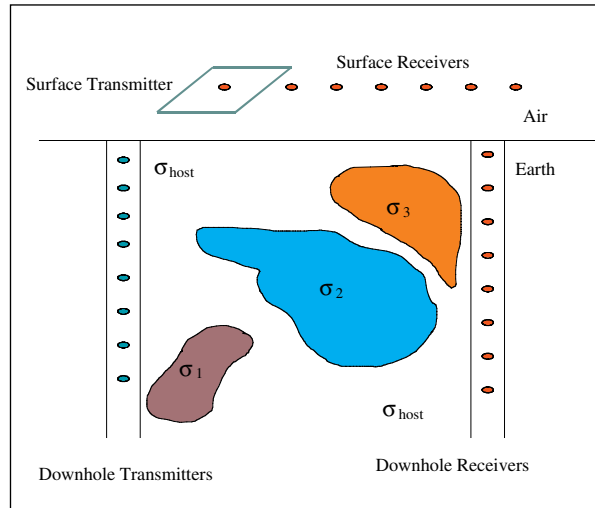


Figure 1. Transmitter antennas and receivers are deployed on the earth's surface as well as in boreholes to map subsurface variations in the electrical conductivity. The transmitters can consist of either electric/magnetic dipoles or loop sources operating at different frequencies of excitation. Other source configurations are possible. The receivers are typically electric/magnetic dipoles that measure the electric/magnetic fields arising from the transmitters, yet altered by the subsurface conductivity. The inverse problem is to recover estimates of the subsurface conductivity from these source–receiver sets.

approximation to the Laplacian (∇^2) operator applied in Cartesian coordinates in order to minimize model curvature in either two or three spatial dimensions. When equation (7) is formed, we implicitly assume that the observed and predicted data have been weighted such that noisy data points are given far less influence in determining the model, which minimizes ϕ . This can be accomplished with an $n \times n$ weighting matrix D , where the quantities $F[m]$ and d^{obs} in equation (7) are given by

$$\begin{aligned} F[m] &= Df[m] \\ d^{\text{obs}} &= Dd^{\text{obs}}. \end{aligned} \quad (8)$$

A typical choice for D would be to form weights based on the inverse of standard deviations of the measurements. In this instance D would be strictly diagonal. Other quantities specified in equation (7) include the reference model, m_{ref} , and the regularization parameter λ , where $\lambda \geq 0$. The regularization parameter trades off the data fit against model smoothness. Its selection requires special care if the model, m , estimated from the inversion process is to be physically reasonable. Selecting a regularization parameter that is too small will produce models that are spatially too rough, but provide superior data fits. On the other hand, selecting it too large will yield highly smoothed models that exhibit poor dependence on the data. Unfortunately, there is no unique approach in its selection. We will discuss our selection procedure for λ shortly.

Computing the gradient $\nabla\phi$ with respect to the model parameters and setting the resulting expression to zero yields the necessary conditions for a minimum in equation (7). With some algebra the k th component of the gradient can be expressed by the following expression:

$$\partial\phi/\partial m_k = \text{Re} \{ \partial F[m]^T / \partial m_k \{ F[m] - d^{\text{obs}} \}^* \} + \lambda w_k^T W(m - m_{\text{ref}}), \quad (9)$$

where w_k denotes the k th column of W and T denotes the transpose operator and Re refers to the real part of the complex argument. The necessary condition $\nabla\phi = 0$ at the functional minimum can then be expressed as

$$\text{Re} \{ J^T(m) (F[m] - d^{\text{obs}})^* \} + \lambda W^T W(m - m_{\text{ref}}) = 0 \quad (10)$$

where $J(m) = \partial F[m]/\partial m$ is the complex sensitivity matrix, and $*$ stands for complex conjugation. The common approach to minimize equation (7) is to use Newton's method to solve the nonlinear set of equations given in equation (10). One can show that the method converges quadratically in the neighbourhood of the functional minimum. Each Newton step amounts to using a quadratic expansion about the current model, m , in order to determine a model step that will reduce the gradient $\nabla\phi$ towards zero. When the functional in equation (7) is of quadratic form, Newton's method will solve equation (10) in one step.

3.2. The Newton iteration

Often it is preferable to apply the Newton iteration directly to the parameter, instead of its perturbed state, to avoid creeping convergence in the Newton iteration (Scales *et al* 1990). This strategy also ensures a smooth sequence of model updates, which is our goal, instead of a sequence of smoothed model perturbations. In addition, it allows for imposition of constraints directly on the model parameters thereby avoiding nonphysical solutions, such as negative conductivity parameters. When the model parameters are determined from a sequence of model perturbations it is possible that the final model is nonphysical, since it is permissible for the model perturbations to be negative. Thus at the i th Newton iterate we seek to determine a model $m^{(i)}$, for which ϕ the norm of $\nabla\phi$ can be reduced. To accomplish this we need the gradient, $g = \nabla\phi$, and the $m \times m$ Hessian matrix, H , which requires both first and second derivatives of $F[m]$ with respect to m in order to solve the system

$$Hm^{(i)} = -g + Hm^{(i-1)}. \quad (11)$$

Newton's method will converge quadratically if the current iterate is sufficiently close to the critical point in equation (10). When it is not, it may be necessary to carry out a weak line search, with backtracking, by adjusting $\mathbf{m}^{(i)}$ according to

$$\mathbf{m}^{(i)} = \mu \mathbf{m}^{(i)} + (1 - \mu) \mathbf{m}^{(i-1)}, \quad (12)$$

where $0 < \mu < 1$ is a parameter chosen to ensure that the norm of the updated gradient has decreased sufficiently (Dennis and Schnabel 1996).

To proceed with the Newton iteration we supply some additional details that link the forward-mapping operator to the inversion methodology discussed thus far; that is, we need to express the \mathbf{g} and \mathbf{H} in terms of the forward problem. Let us first consider the gradient.

The predicted data, $F[\mathbf{m}]$, arise from a linear combination of the electric field \mathbf{E} , that has been determined on the discretization grid of size N for a given source specified in the forward problem, with a linear interpolation operator, \mathbf{Q} . Depending on whether electric or magnetic field types are of interest, the operator \mathbf{Q} acts upon \mathbf{E} and two results are possible: the result is (1) to interpolate the electric field from the grid to receiver locations or (2) to compute the discrete curl of the electric field on the grid and interpolate the result to the receiver locations; hence predicted magnetic field measurements are possible within this framework. In either instance, the predicted field that results is then weighted according to equation (8). Thus we write

$$F[\mathbf{m}] = \mathbf{Q}\mathbf{E}, \quad (13)$$

where \mathbf{Q} is independent of \mathbf{m} , includes the effect of the data weighting matrix \mathbf{D} , and exhibits dimensions $n \times N$ with $n \ll N$. Thus the data sensitivity to the k th model parameter can be expressed as

$$\partial F[\mathbf{m}]/\partial m_k = \mathbf{Q}\partial \mathbf{E}/\partial m_k, \quad (14)$$

where, following Newman and Alumbaugh (1997), $\partial \mathbf{E}/\partial m_k$ is expressed as

$$\partial \mathbf{E}/\partial m_k = \mathbf{K}^{-1}(\partial \mathbf{S}/\partial m_k - \partial \mathbf{K}/\partial m_k \mathbf{E}). \quad (15)$$

When the forward problem in equation (3) is expressed in terms of the scattered fields, the source vector \mathbf{S} will depend linearly on the model parameters and is therefore included in equation (15). With a total field solution, however, $\partial \mathbf{S}/\partial m_k$ would be zero. Thus the k th column of the data sensitivity/Jacobian matrix, \mathbf{J} , is written as

$$\mathbf{J}_k = \mathbf{Q}\mathbf{K}^{-1}(\partial \mathbf{S}/\partial m_k - \partial \mathbf{K}/\partial m_k \mathbf{E}). \quad (16)$$

Let us define an $N \times m$ matrix \mathbf{G} , where

$$\mathbf{G} = \{(\partial \mathbf{S}/\partial m_1 - \partial \mathbf{K}/\partial m_1 \mathbf{E}), (\partial \mathbf{S}/\partial m_2 - \partial \mathbf{K}/\partial m_2 \mathbf{E}), \dots, (\partial \mathbf{S}/\partial m_m - \partial \mathbf{K}/\partial m_m \mathbf{E})\}. \quad (17)$$

Hence we can express \mathbf{J} with matrix products involving \mathbf{Q} , \mathbf{K}^{-1} and \mathbf{G} :

$$\mathbf{J} = \mathbf{Q}\mathbf{K}^{-1}\mathbf{G}. \quad (18)$$

Using equations (10), (13) and (18) we can then express the gradient as

$$\mathbf{g} = \text{Re} \{ \mathbf{G}^T \mathbf{K}^{-1} \mathbf{Q}^T \{ \mathbf{Q}\mathbf{E} - \mathbf{d}^{\text{obs}} \}^* \} + \lambda \mathbf{W}^T \mathbf{W}(\mathbf{m} - \mathbf{m}_{\text{ref}}), \quad (19)$$

where we have employed the fact that

$$\mathbf{K}^{-T} = \mathbf{K}^{-1} \quad (20)$$

since \mathbf{K} is complex-symmetric.

We derive the Hessian by differentiating equation (9) with respect to the j th model parameter. That is

$$\partial^2 \phi / \partial m_j \partial m_k = \text{Re} \{ \partial \mathbf{F}^H[\mathbf{m}] / \partial m_j \partial \mathbf{F}[\mathbf{m}] / \partial m_k + \{\mathbf{F}[\mathbf{m}] - \mathbf{d}_{\text{obs}}\}^H \partial^2 \mathbf{F}[\mathbf{m}] / \partial m_j \partial m_k \} + \lambda \mathbf{w}_k^T \mathbf{w}_j. \quad (21)$$

Here the (j, k) entry of the Hessian is given by $\mathbf{H}_{jk} = \partial^2 \phi / \partial m_j \partial m_k$. In this expression, the forward-mapping operator, $\mathbf{F}[\mathbf{m}]$, and the data sensitivities, $\partial \mathbf{F}^H[\mathbf{m}] / \partial m_j$ and $\partial \mathbf{F}[\mathbf{m}] / \partial m_k$, can be readily evaluated from equations (13)–(15). We now express $\partial^2 \mathbf{F}[\mathbf{m}] / \partial m_j \partial m_k$ in terms of the forward problem. First we differentiate equation (14) with respect to the j th model parameter, which yields

$$\partial^2 \mathbf{F}[\mathbf{m}] / \partial m_j \partial m_k = \mathbf{Q} \partial^2 \mathbf{E} / \partial m_j \partial m_k. \quad (22)$$

Equation (3) is then differentiated with respect to the j th and k th model parameters, where

$$\partial^2 \mathbf{E} / \partial m_j \partial m_k = \mathbf{K}^{-1} \{ \partial^2 \mathbf{S} / \partial m_j \partial m_k - \partial^2 \mathbf{K} / \partial m_j \partial m_k \mathbf{E} - \partial \mathbf{K} / \partial m_k \partial \mathbf{E} / \partial m_j - \partial \mathbf{K} / \partial m_j \partial \mathbf{E} / \partial m_k \}. \quad (23)$$

Newman and Alumbaugh (1997) demonstrate that the matrix $\partial \mathbf{K} / \partial m_j$ and vector $\partial \mathbf{S} / \partial m_j$ are also highly sparse with a maximum of twelve nonzero entries. Moreover, \mathbf{K} is linear in the model parameters, thus $\partial \mathbf{K} / \partial m_j$ does not depend on the model parameters for all j , it only depends on the spatial grid intervals employed in finite-difference mesh. Similar reasoning can be applied to \mathbf{S} when a scattered field solution is employed in the forward problem; otherwise, \mathbf{S} , as specified in a total field solution, is independent of the model parameters. In all cases, however, $\partial^2 \mathbf{S} / \partial m_j \partial m_k$ and $\partial^2 \mathbf{K} / \partial m_j \partial m_k$ are zero and are dropped from equation (23). Finally, equation (22) can be expressed with the aid of equations (15) and (23) as

$$\partial^2 \mathbf{F}[\mathbf{m}] / \partial m_j \partial m_k = -\mathbf{Q} \mathbf{K}^{-1} \{ \partial \mathbf{K} / \partial m_k \mathbf{K}^{-1} (\partial \mathbf{S} / \partial m_j - \partial \mathbf{K} / \partial m_j \mathbf{E}) + \partial \mathbf{K} / \partial m_j \mathbf{K}^{-1} (\partial \mathbf{S} / \partial m_k - \partial \mathbf{K} / \partial m_k \mathbf{E}) \}. \quad (24)$$

Next, incorporating equations (13)–(15), (20) and (24) along with the identity

$$\text{Re} \{ \partial \mathbf{F}^H[\mathbf{m}] / \partial m_j \partial \mathbf{F}[\mathbf{m}] / \partial m_k \} = \text{Re} \{ \partial \mathbf{F}^T[\mathbf{m}] / \partial m_j (\partial \mathbf{F}[\mathbf{m}] / \partial m_k)^* \} \quad (25)$$

into equation (21), we finally obtain the (j, k) entry of the Hessian,

$$\begin{aligned} \mathbf{H}_{jk} = & \text{Re} \{ (\partial \mathbf{S} / \partial m_j - \partial \mathbf{K} / \partial m_j \mathbf{E})^T \mathbf{K}^{-1} \mathbf{Q}^T \{ \mathbf{Q} \mathbf{K}^{-1} (\partial \mathbf{S} / \partial m_k - \partial \mathbf{K} / \partial m_k \mathbf{E}) \}^* \\ & - \{ \mathbf{Q} \mathbf{E} - \mathbf{d}^{\text{obs}} \}^H \mathbf{Q} \mathbf{K}^{-1} \{ \partial \mathbf{K} / \partial m_k \mathbf{K}^{-1} (\partial \mathbf{S} / \partial m_j - \partial \mathbf{K} / \partial m_j \mathbf{E}) \\ & + \partial \mathbf{K} / \partial m_j \mathbf{K}^{-1} (\partial \mathbf{S} / \partial m_k - \partial \mathbf{K} / \partial m_k \mathbf{E}) \} \} + \lambda \mathbf{w}_k^T \mathbf{w}_j. \end{aligned} \quad (26)$$

A check is available on equation (26) with the aid of equation (16), whereby we can replace the leading term in equation (26) with

$$\mathbf{J}_j^T \mathbf{J}_k^* = (\partial \mathbf{S} / \partial m_j - \partial \mathbf{K} / \partial m_j \mathbf{E})^T \mathbf{K}^{-1} \mathbf{Q}^T \{ \mathbf{Q} \mathbf{K}^{-1} (\partial \mathbf{S} / \partial m_k - \partial \mathbf{K} / \partial m_k \mathbf{E}) \}^*. \quad (27)$$

Thus, it is straightforward to show that equation (26) displays the required symmetry condition

$$\mathbf{H}_{jk} = \mathbf{H}_{kj}, \quad (28)$$

since

$$\text{Re} \{ \mathbf{J}_j^T \mathbf{J}_k^* \} = \text{Re} \{ \mathbf{J}_k^T \mathbf{J}_j^* \}. \quad (29)$$

Let us now define a vector \mathbf{v}^T with N column entries, where

$$\mathbf{v}^T = -(\mathbf{Q} \mathbf{E} - \mathbf{d}^{\text{obs}})^H \mathbf{Q} \mathbf{K}^{-1} \quad (30)$$

along with the $m \times N$ matrix \mathbf{V} such that

$$\mathbf{V} = \{ \mathbf{v}^T \partial \mathbf{K} / \partial m_1, \mathbf{v}^T \partial \mathbf{K} / \partial m_2, \dots, \mathbf{v}^T \partial \mathbf{K} / \partial m_m \}^T. \quad (31)$$

Using equations (16)–(18) and (31) we may then express equation (26) in matrix form,

$$\mathbf{H} = \text{Re} \{ \mathbf{J}^T \mathbf{J}^* + \mathbf{V} \mathbf{K}^{-1} \mathbf{G} + \mathbf{G}^T \mathbf{K}^{-1} \mathbf{V}^T \} + \lambda \mathbf{W}^T \mathbf{W} \quad (32)$$

where

$$\mathbf{J}^T \mathbf{J}^* = \mathbf{G}^T \mathbf{K}^{-1} \mathbf{Q}^T \{ \mathbf{Q} \mathbf{K}^{-1} \mathbf{G} \}^*. \quad (33)$$

It is straightforward to generalize these expressions for \mathbf{g} and \mathbf{H} for multiple source fields. The gradient and the Hessian are simply the sum of the gradients and Hessians arising from each source as applied in equation (3).

3.3. Selecting the regularization parameter

Many strategies have been advanced for selecting the regularization parameter, but there appears to be no unique approach. Here we refer the reader to the following works on the subject: Constable *et al* (1987), deGroot-Hedlin and Constable (1990), Asher *et al* (1995), Newman (1995), Newman and Alumbaugh (1997) and Smith *et al* (1999). In our experience, a continuation or ‘cooling’ approach has worked well for the problem. The basic idea is to start with a relatively large value of λ , where we solve an almost quadratic problem in equation (7). We then reduce λ and move to a problem where the data fitting requirement weighs more in equation (7). A new minimization problem is then solved. This process of reducing λ continues until an acceptable data misfit, given by

$$\{(\mathbf{F}[\mathbf{m}] - \mathbf{d}^{\text{obs}})\}^H \{(\mathbf{F}[\mathbf{m}] - \mathbf{d}^{\text{obs}})\} < \text{Tot} \quad (34)$$

is achieved. Experience shows that this procedure stabilizes the inversion process at the outset by guarding against arbitrarily rough models that are nonphysical. Following Newman and Alumbaugh (1997) we select λ as follows: at each inversion iteration we first estimate the largest eigenvalue of the nonregularized part of the Hessian matrix in equation (32). This can be done by computing the value, r_{sum} , which is the largest row sum of the matrix

$$\text{Re} \{ \mathbf{J}^T \mathbf{J}^* + \mathbf{V} \mathbf{K}^{-1} \mathbf{G} + \mathbf{G}^T \mathbf{K}^{-1} \mathbf{V}^T \}. \quad (35)$$

The regularization parameter, λ , is then determined at each inversion iteration by

$$\lambda = r_{\text{sum}} / 2^{(i-1)}. \quad (36)$$

Here the index i refers to the current inversion iteration. At the early stages of the inversion process, selecting λ using equation (36) produces model updates that are influenced by the larger eigenvalue–eigenvector pairs associated with the nonregularized part of the Hessian matrix along with the smoothing constraint imposed upon the problem. Thus parts of the model structure that are well determined by the data are first admitted into the inverse solution. As the iteration procedure continues, λ is reduced and more structure is admitted into the model. It is possible during this procedure to reduce λ too much during the terminal stages of the inversion iteration and this will cause ϕ to increase in equation (7). At this point we fix λ at the previous inversion iteration value for which ϕ decreased and continue the iteration. Our stopping criteria are as follows: (1) convergence of the iteration, (2) the data are fit to within the noise level in the measurements, or (3) some preset iteration limit has been attained.

4. Strategies for 3D problems

4.1. Imposition of constraints

Because 3D inverse problems are underdetermined and use data sets that are undersampled and noisy, they are inherently ill-posed. While regularization and inverting against a reference

model can ameliorate the instability of the problem, imposition of additional constraints can be of great value. Independent information is often available about a site and should be employed in constructing a solution to the inverse problem. A solution that incorporates this information should further reduce its ambiguity. In this section we consider imposition of inequality constraints that place bounds on the model parameters as well as the incorporation of prior information on known geological structures within the regularization matrix, \mathbf{W} .

An important constraint on the electrical conductivity is that it must be positive. It is therefore advisable to formulate our inverse solutions in which negative model parameters are excluded. We have had success in imposing this type of constraint for 3D problems through a log parametrization, which can also be used to impose lower bounding constraints on the parameters. Let us define a new parameter u_k that is related to the k th model parameter m_k as follows:

$$u_k = \ln(m_k - lb_k), \quad (37)$$

where lb_k is a lower bounding constraint on the k th model parameter, m_k such that $m_k > lb_k$. We also can express m_k in terms of u_k , via the expression

$$m_k = e^{u_k} + lb_k. \quad (38)$$

Hence

$$\partial m_k / \partial u_k = m_k - lb_k. \quad (39)$$

To reformulate the inverse problem for log parameters, defined by equation (37), we employ the chain rule and use equation (39) to modify the matrices \mathbf{G} and \mathbf{V} as follows:

$$\mathbf{G} = \{(m_1 - lb_1)(\partial \mathbf{S} / \partial m_1 - \partial \mathbf{K} / \partial m_1 \mathbf{E}), \dots, (m_m - lb_m)(\partial \mathbf{S} / \partial m_m - \partial \mathbf{K} / \partial m_m \mathbf{E})\} \quad (40)$$

and

$$\mathbf{V} = \{(m_1 - lb_1)\mathbf{v}^T \partial \mathbf{K} / \partial m_1, (m_2 - lb_2)\mathbf{v}^T \partial \mathbf{K} / \partial m_2, \dots, (m_m - lb_m)\mathbf{v}^T \partial \mathbf{K} / \partial m_m\}^T. \quad (41)$$

Thus the model update, defined by equation (11), is now determined from

$$\mathbf{H}_{\ln} \mathbf{u}^{(i)} = -\mathbf{g}_{\ln} + \mathbf{H}_{\ln} \mathbf{u}^{(i-1)} \quad (42)$$

where \mathbf{g}_{\ln} and \mathbf{H}_{\ln} are based on equations (19) and (32) that incorporate the changes in equations (40) and (41) with the current and reference model in equation (19) replaced by their log counterparts. Once $\mathbf{u}^{(i)}$ has been determined, $\mathbf{m}^{(i)}$ is determined using equation (38). While hyperbolic transformations are available to enforce both upper and lower bounding constraints on the 3D problem, we advise that they be avoided because, in our experience, they greatly increase the nonlinearity and instability of the problem. Recent advances in optimization theory suggest that limited memory quasi-Newton methods with bound constraints appear to be a promising approach for 3D problems. We refer the reader to the works of Lin and Moore (1999) for more information.

By altering \mathbf{W} , we can preserve known structural boundaries within the inversion domain, and still impose smoothness constraints elsewhere where we have no direct information. An example of such an instance would be the top surfaces of sub-salt bodies determined from seismic experiments (Hoversten *et al* 1998). To improve the resolution of these features, for EM inversion investigations, it is desirable to incorporate tears in the regularization matrix \mathbf{W} at the known surfaces when we expect rapid changes in the electrical conductivity. Imposition of a tear into \mathbf{W} eliminates the smoothness constraint across that surface, but it still preserves the symmetry in \mathbf{W} . For a given conductivity parameter/cell within the inversion domain, a row of the matrix \mathbf{W} is constructed for the 3D problem with a 7-point Laplacian stencil.

This stencil couples the conductivity of the cell to its nearest neighbours along the Cartesian coordinate axis, thereby providing the smoothness constraint. However, when a surface is imposed between this cell and any of its neighbours, no coupling is allowed between those cells. Thus, the 7-point stencil is reduced accordingly.

4.2. Computational considerations

For 3D problems, forming the Hessian and directly solving the model update via equation (11) is computationally prohibitive. On the other hand, matrix–vector products involving the Hessian are not that expensive. Hence Newton–Krylov methods offer a reasonable approach to iteratively solving equation (11) to some predetermined error level. The CG method is the best known of the Newton–Krylov methods and can be applied directly to equation (11) since the Hessian is symmetric positive definite (Mackie and Madden 1993, Newman and Alumbaugh 1997, Haber *et al* 1999a). To use this strategy we observe that matrix–vector products involving the regularization matrix, \mathbf{W} , are easy to compute and require minimal storage because \mathbf{W} is highly sparse, requiring only seven nonzero entries per row to be stored. Inspection of equation (32) then shows that three forward solutions of equation (3) per source at a fixed frequency are all that are needed to complete one iteration of a CG algorithm. A similar result is demonstrated in Haber *et al* (1999a) when a Newton–Krylov/CG method is employed for computing the full Newton step. Thus for some real vector \mathbf{x} , we would be required to solve the following problems:

$$\mathbf{K}\mathbf{y} = \mathbf{G}\mathbf{x} \quad (43)$$

$$\mathbf{K}\mathbf{z} = \mathbf{Q}^T \{\mathbf{Q}\mathbf{y}\}^*, \quad (44)$$

and

$$\mathbf{K}\mathbf{u} = \mathbf{V}^T \mathbf{x}. \quad (45)$$

To initialize the CG algorithm, five additional forward solutions per source and frequency are required for specifying the right-hand side of equation (11), $-\mathbf{g} + \mathbf{H}\mathbf{m}^{(i-1)}$. The first is to determine the electric field, \mathbf{E} , with equation (3) and the second is

$$\mathbf{K}\mathbf{r} = \mathbf{Q}^T \{\mathbf{Q}\mathbf{E} - \mathbf{d}^{\text{obs}}\}^*, \quad (46)$$

which is used for computing the gradient in equation (19). The third, fourth and fifth arise from the matrix–vector product $\mathbf{H}\mathbf{m}^{(i-1)}$ and are given by equations (43)–(45), where \mathbf{x} has been replaced by $\mathbf{m}^{(i-1)}$.

Let us define n_{rel} as the number of CG relaxation steps needed to produce an acceptable model update and N_{tx} as the number of sources applied in the problem at a fixed frequency. Thus the total number of forward modelling solutions per frequency needed for the model update is given by the expression, $5N_{\text{tx}} + 3n_{\text{rel}}N_{\text{tx}}$. A common approach taken to reduce the computational burden is to invoke a Gauss–Newton approximation by neglecting terms involving the matrix \mathbf{V} in equation (32). Thus solution of equation (45) is no longer necessary. Justification for this assumption is based on the observation that as we approach the functional minimum in equation (7), \mathbf{V} will vanish because, in equation (30), $\mathbf{v}^T \rightarrow 0$, since $\mathbf{Q}\mathbf{E} \rightarrow \mathbf{d}^{\text{obs}}$. In this case the number of forward modelling applications required for the model update reduces to $4N_{\text{tx}} + 2n_{\text{rel}}N_{\text{tx}}$ per frequency.

Usually tens of matrix–vector products are required for computing the model update in equation (11) with conjugate gradients. Thus the number of forward-modelling applications can become excessive if a large number of CG relaxation steps are needed; each relaxation step requires two or three forward-modelling applications per source at each distinct frequency. Fortunately, we can avoid this difficulty when the number of receivers is modest in number.

Newman and Alumbaugh (1999) showed that, in this instance, it is better to compute all necessary forward solutions first before applying the CG algorithm to compute the model update. Assuming a Gauss–Newton approximation, where

$$\mathbf{H} \approx \text{Re} \{ \mathbf{J}^T \mathbf{J}^* \} + \lambda \mathbf{W}^T \mathbf{W}, \quad (47)$$

it is necessary to precompute the electric field, \mathbf{E} , for each source along with the adjoint electric fields, ${}^a\mathbf{E}$, arising from each and every receiver location assigned to that source on the finite-difference mesh; we consider a source to be distinct in both position and frequency. For our purposes, sources occupying the same physical location but operating at different frequencies are considered distinct. If we define an $n \times N$ matrix \mathbf{U}^T , where

$$\mathbf{U}^T = \{ {}^a\mathbf{E}_1, {}^a\mathbf{E}_2, \dots, {}^a\mathbf{E}_n \}^T, \quad (48)$$

the adjoint electric fields can be obtained by solving the block system

$$\mathbf{Q}\mathbf{K}^{-1} = \mathbf{U}^T. \quad (49)$$

Since there are n rows of \mathbf{Q} , solving the block system involves n additional forward solves for each source. Additional computational savings can be realized within this framework when there are identical sets of receivers for different sources, operating at a common frequency. This is a prevalent configuration utilized for cross-well measurements. Let us assume we have l unique receiver positions corresponding to these sources. A unique receiver position consists of a specific field component made at a site. Thus the total number of forward solutions needed for the model update is $N_{\text{tx}} + N_{\text{rx}}$, where N_{tx} and N_{rx} are the total number of sources and unique receivers applied in the inverse problem at a given frequency. Hence for multiple-frequency data sets the number of forward solutions scales directly with the number of operating frequencies. It was this type of implementation for determining the model update that Alumbaugh and Newman (1997) utilized to successfully invert a 3D cross-well field data set.

5. Strategies for 2D problems

5.1. Imposition of constraints

For 2D problems, we can explicitly form \mathbf{H} , thus upper and lower bounding constraints can be readily imposed upon the Newton iteration in equation (11) using quadratic programming (Fletcher and Jackson 1974). Thus, the Newton iteration is defined by

$$\mathbf{H}\mathbf{m}^{(i)} = -\mathbf{g} + \mathbf{H}\mathbf{m}^{(i-1)}. \quad (50)$$

subject to

$$l_b \leq \mathbf{m}^{(i)} \leq \mathbf{u}_b \quad (51)$$

where l_b and \mathbf{u}_b are the upper and lower bounding constraints. It is assumed that these constraints are fixed and do not change with the model update. We have found that the inequality constraints are more robust than logarithmic constraints. They restrict the conductivity to lie within a range provided by prior information, such as well logs, and greatly reduce solution ambiguity. However, when using inequality constraints, one must be careful not to overconstrain the problem (Eaton 1987), since the solution can pass through unfeasible regions of parameter space as it converges upon a feasible solution.

Incorporation of prior information on known geological structural boundaries within the regularization matrix is easy to implement and follows similarly from the 3D problem discussed above.

5.2. Computational considerations

As already mentioned above, in 2D problems we can directly form \mathbf{H} since the number of model parameters are far fewer for 2D problems than for 3D problems, at least by an order of magnitude. Employing a Gauss–Newton approximation, given by equation (47), we construct \mathbf{H} by precomputing the electric field, \mathbf{E} , for each source along with a set of adjoint electric fields, ${}^a\mathbf{E}$, arising from the receivers acting as sources at each and every frequency. To reduce the computational burden, we note that identical receiver sets are often applied to different source locations for 2D problems. Hence we only need to compute these adjoint fields once for each frequency.

6. Other computational strategies

We have reviewed computational strategies for 3D and 2D EM inverse problems. The approach we have adopted in the formulation of these problems is to set up the solutions within a constrained framework, where the forward problems required for each Newton step are solved to within some predetermined accuracy. Thus the predicted data determined from the model update satisfies the forward-modelling equations to within an acceptable accuracy level. In an alternative approach, we can formulate the Newton iteration, using the all-in-one approach (Heinkenschloss 1996). In this approach, we relax the constraint that we precisely solve the forward problem until convergence of the Newton iteration. Here the control variable (the electric field in our case) is also cast as an optimization unknown, along with the model parameters and a set of Lagrange multipliers, which ensure that the electric field will satisfy the forward problem upon convergence of the Newton iteration. This approach has appeal when the forward problem is difficult to solve and multiple solutions of it are needed to arrive at an inverse solution, as in our case. We point out, however, that because we are employing iterative Krylov methods in the forward problem as well as in the 3D inverse problem, it is not necessary to precisely solve these problems at the early stages of the iteration procedure. As an example, Newman and Alumbaugh (1997) showed that early in the Newton iteration, the number of CG relaxation steps only need be a small fraction compared with those at the latter iterations for an acceptable model update. Moreover, in the terminal stages of the iteration procedure one finds convergence in the CG solver to a predetermined error level to occur rapidly, requiring only a few CG relaxation steps. Finally, we foresee the implementation of a multiple right side QMR algorithm (Freund and Malhotra 1995) to realize additional efficiencies in solving the forward problem for multiple sources operating at a common frequency. Nevertheless, the all-in-one approach looks promising for the types of inverse problems discussed in this paper, where it may be possible to solve the inverse problem without calculating solutions to the forward problem even once (Haber *et al* 1999b). A danger with this approach, however, is that by fully relaxing the forward-modelling constraint the Newton iteration may diverge.

7. Field examples

Cross-well EM measurements are useful for monitoring the conductivity changes in reservoirs over time and the associated changes in subsurface saturation arising from the injection of steam, water or CO₂ to mobilize oil reserves for increased production. The review of Wilt *et al* (1999) describes the instrumentation and field procedures for making cross-well measurements. In the processing of cross-well data, the inversion process is essential in producing a map of conductivity changes within the inter-well region. The conductivity/saturation changes provide important information on how to efficiently produce the field and extract more reserves.

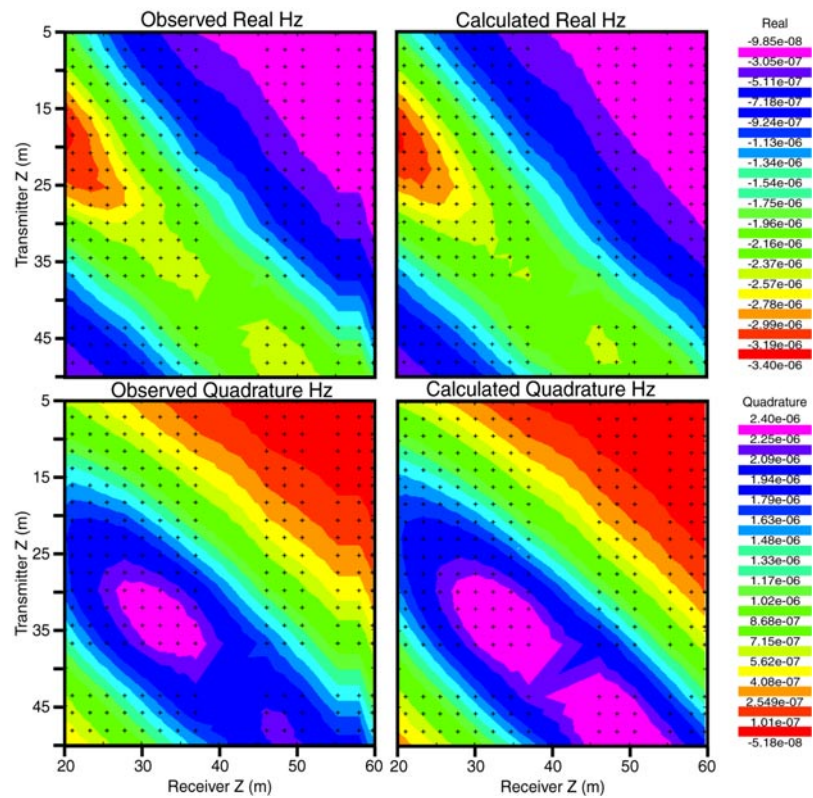


Figure 2. Observed real and quadrature vertical magnetic field (left-hand side) in amps m^{-1} measured in well 1254. The right-hand side shows the calculated vertical magnetic field from the inverse model shown in figure 3. The operating frequency is 9600 Hz.

Cross-well EM is also being employed to map near-surface geology for environmental site characterization. We consider two examples of these applications, in 2D, below.

7.1. Environmental site characterization

One emerging application of cross-well EMs is in subsurface characterization of chemically contaminated sites. A primary concern is mapping sand channels that are conduits for fluid movement, thus providing pathways for moving contaminants away from their point of origin. In the vadose zone, sands are generally more resistive than clay-rich shales. Below the water table the relative conductivity of sand and shale depends on the fluid type within the sand. In relatively freshwater environments, sand is usually more resistive than surrounding shale. The electrical contrast between channel sands and their surroundings provides a means of mapping using electrical techniques.

As part of a site characterization study performed at Lawrence Livermore National Laboratory, cross-well EM measurements were made between a number of shallow boreholes. This site has had volatile chemical wastes (VOCs) dumped at spots during the period of the 1940s, when it was a Naval Air Force base, before the Department of Energy took it over as a National Laboratory. Due to concerns of natural aquifer water transporting these VOCs in the shallow subsurface, the Department of Energy (DOE) undertook the task of site remediation.

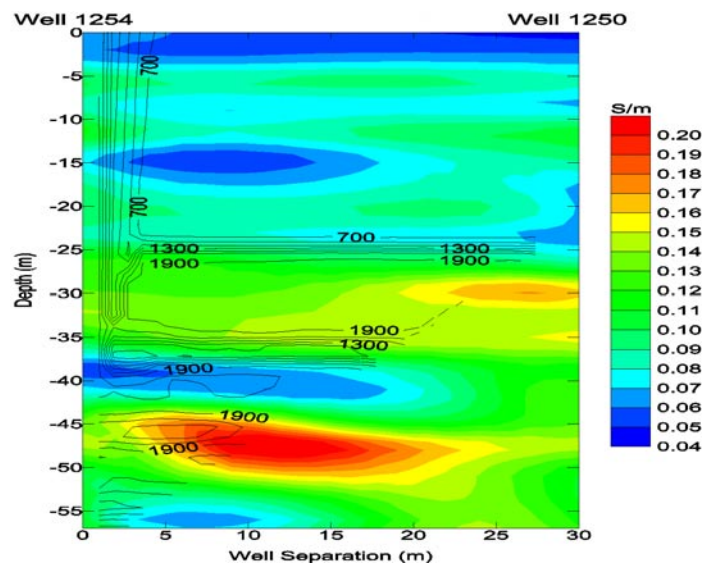


Figure 3. 2D conductivity section between wells 1254 (0 offset) and 1250 (30 m offset). Velocity section derived from vertical seismic profiles overlaid as contours. The water table is at 24 m where there is a sharp velocity and conductivity gradient. The top of the sand channel is marked by the low-velocity zone at 37 m.

This consisted of mapping and quantifying where these contaminants were being transported by the natural aquifer flow in this region. Many exploratory boreholes were drilled down to depths of about 65 m.

Part of the characterization process was to try and map the extent of sand aquifers between boreholes. Geologic mapping and contouring of observations made in adjacent boreholes indicated that a sand aquifer observed in well W-1254 between 36 and 42 m depth did not extend to the W-1250 well. Cross-well EM measurements were made in wells W-1250 (transmitters) and W-1254 (receivers) to see whether the lateral extent of the aquifer could be determined.

A 9.6 kHz vertical magnetic dipole transmitter was deployed down well W-1250 and a vertical component magnetic receiver was deployed in W-1254. Multiple recordings of different source and receiver depth levels were made, by continuously moving the transmitter coil, for fixed positions of the receiver coil every 2.3 m. This sampling interval was chosen so as to place the receiver between metallic collar rings around the well casings. The collars caused coupling and detuning effects when the receiver coils were placed near them. High-voltage cables and communication lines (which saturated the receiver coils) in the weathered layer close to the boreholes also made it impossible to deploy the receiver coil shallower than a depth of 17 m to 27 m, depending on the proximity of the cables. In this example, we note that the field is attenuated by nearly two skin depths between the wells, assuming a background media of 0.1 S m^{-1} , typical of the site. This should allow for sufficient sensitivity to conductivity variations between the wells (Alumbaugh and Morrison 1995).

The boreholes, in the vicinity of the sand aquifer zones, had metallic screens that extended for 3 m with 1.5 m metal risers above and below the screened interval. No transmitter or receivers locations were situated within these conductive sections of the boreholes. This reduced, though it did not eliminate, the ability to image the resistive freshwater aquifer layer intersecting the boreholes at the screened intervals. The left-hand panels of figure 2 show the

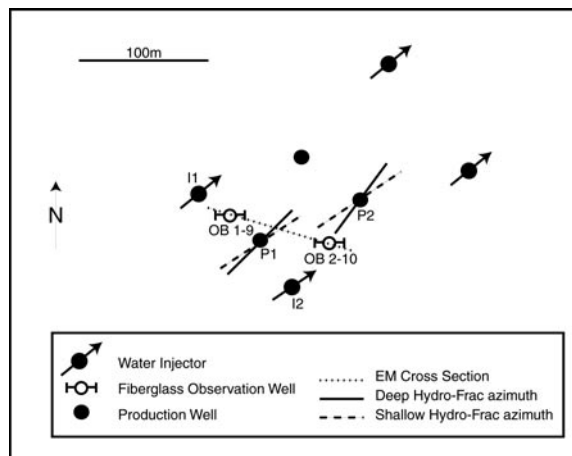


Figure 4. Map of well locations for cross-well EM time lapse study at Lost Hills. The cross-well EM experiment was done between two fibreglass-cased observation wells OB 1-9 and OB 2-10. The first cross-well EM survey was conducted in April 1997 just prior to the start of water injection. A second survey was run 17 months later in September 1998. During this time early water production occurred in the P2 producer.

real (in-phase) and quadrature (out-of-phase) vertical magnetic field data collected in the 1254 well. The calculated data from the inverse model shown in figure 3 are shown in the right-hand panels of figure 2. The observed data were assigned an observation error of 5%.

The inversion of the observed data used a starting model built by linearly interpolating the conductivity from well logs at wells 1250 and 1254. Because there was no apparent dip on the layering between these wells the interpolation was horizontal. The starting model was used as a reference model and perturbations about this model were determined. The weights placed on each data point were set to 5% of the maximum vertical magnetic field amplitude observed in the measured data. The calculated data shown in the right-hand side of figure 2 fit the observed data (left-hand side of figure 2) to a root mean squared (RMS) error value of 1.2.

There are two major features in the inverse model shown in figure 3. First, the water table is clearly shown as the gradation, across the entire section, in conductivity around a depth of 24 m from lower values to higher values. Secondly, the low-conductivity sand channel observed in well 1254 at a depth between 36 and 42 m does not extend to well 1250, but truncates approximately 20 m from the 1254 well. The inter-well resolution is not sufficient to determine whether or not the channel truncates abruptly or gradually grades from sand to shale. It is also significant that the conductivity section derived from the cross-well EM measurements coincides closely with a velocity section derived from a vertical seismic profiles (VSPs) shot in the 1254 well. We have overlaid the contours of velocity on figure 3. Here an increase in velocity and a decrease in conductivity mark the water table transition. At the top of the sand channel there is a marked low-velocity zone, probably the result of partial saturation. Zones of partial saturation are often seen at the top of aquifers which have experienced cyclic saturation and desaturation due to movement in the water table. Overall, this cross-well experiment was considered quite successful in mapping the lateral extent of the aquifer.

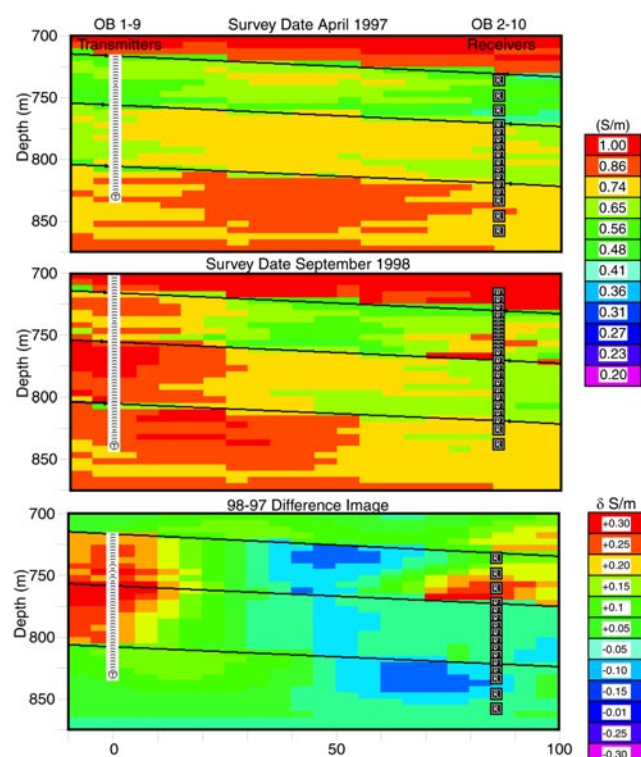


Figure 5. Cross-well EM time-lapse inversions at Lost Hills Oil Field. Upper panel: inverse conductivity section for the April 1997 data set. Middle panel: inverse conductivity section for the September 1998 data set. Bottom panel: difference image, 1998 conductivity section minus 1997 conductivity section. The black lines represent the unit tops used to guide the interpolation of the conductivity logs to form the starting model for the April 1997 inversion.

7.2. Petroleum reservoir characterization

As part of a pilot study of water injection in a portion of the Lost Hills Oil Field, California's Central Valley, a time lapse cross-well EM experiment was performed by EM Instruments Inc. Figure 4 shows a well location map for the project. A vertical magnetic dipole transmitter operating at 1000 Hz was run in the OB 1-9 well while a vertical magnetic field receiver was used in the OB 2-10 well.

The layout is a standard 'five-spot' pattern in which each producing well is surrounded by four water injectors. As production progresses additional producers are sometimes added to enhance production. The method of production is to hydraulically fracture 'hydro-frac' the production and injection wells. The fractures produced by the hydro-frac run in a southwest to northeast direction, as shown in figure 4. The ideal scenario is for the water to move out from these fractures and sweep oil between the rows of injectors to the producers situated in between. This scenario is often not achieved, with water 'disappearing', leaving unswept areas of high residual oil. The purpose of the cross-well EM measurements was to determine whether cross-well EM could image the reservoir and answer two basic questions: (1) where is the residual oil and (2) where does the water go?

The reservoir in this area of the field is comprised of an upper, less conductive, unit and a lower, more conductive, unit. There is a slight dip to the southeast. Deep induction logs

run in the two observation wells prior to water injection were used to construct the starting model for the inversion of the first data set. The conductivity from the logs at the OB 1-9 and OB 2-10 were interpolated along a dipping surface between the two wells to construct the starting model. The starting model constructed from the interpolated well logs was used as a reference model and perturbations about this reference were determined. Observation errors were assigned at 5% of the maximum vertical magnetic field amplitude.

The upper panel of figure 5 shows the inverted conductivity cross section for the April 1997 data set. This model was next used as the starting and reference model for the inversion of the September 1998 data set resulting in the model shown in the middle panel of figure 5. The difference between the two inverse models is shown in the bottom panel of figure 5. The difference image highlights the changes in the reservoir over the 17 months between surveys. The RMS data misfits were 0.98 and 1.2 for the April 1997 and September 1998 inversions respectively.

There are three major features of the difference image. First, there is a large area around the OB 1-9 well where the conductivity has increased. Second, the conductivity has decreased in the region between the two wells. Third, there is a small zone at the base of the upper unit where the conductivity has increased around the OB 2-10 well. The general increase in conductivity around the OB 1-9 well represents the movement of conductive water from the nearby I1 injector. The decrease in conductivity in the inter-well region represents the increase in oil saturations as oil is swept to the P1 producer. The increase in conductivity in the bottom of the upper unit at the OB 2-10 well represents direct water communication through a fracture in the upper unit between the I2 injector and the P2 producer.

The difference image produced by these surveys confirms the observations of water and oil production in the surrounding wells as well as the premature water breakthrough in the P2 producer. This demonstration survey is considered quite successful and has resulted in continuing cross-well EM surveys for monitoring within the reservoir.

8. Discussion and conclusions

Advances in available computer power have allowed for the development of multidimensional EM forward and inverse algorithms based on the complete physics of EM wave propagation and scattering. Thus 3D and 2D full waveform EM inversion is now a reality. Advances in instrumentation, including three-component magnetic field sensors, have also given us the capability of acquiring high-quality EM data sets, which can now routinely be interpreted in two and three dimensions using high-end desktop workstations for small data sets and high-performance parallel computers for extremely large applications. These advances have come rapidly. Only a few years ago researchers were concentrating on inverse solutions based on approximate forward solutions as a way of making data interpretations tractable; now 'exact' full field solutions can be used, reducing the assumptions and improving the accuracy of the interpreted models.

We anticipate that new strategies for solving 2D and 3D EM inverse problems will become available in the coming years. An area that looks highly promising is the development of joint inverse solutions that incorporate the multi-physics responses. For example, a joint inverse solution that employs EM and seismic data has great appeal. It can greatly reduce solution ambiguities that arise when only a single type of measurement is employed in the inversion process. In a joint inversion, the poorer resolving power of the EM method can be mitigated by incorporation of higher-resolution information provided by the seismic data. On the other hand, seismic methods do not respond as well as EM methods to variations in subsurface saturation. Hence, incorporation of EM data in a seismic experiment for mapping saturation

changes would help reduce solution uncertainties there. Because both methods sense common geological features, but in a different manner, one would expect improvements in our ability to image subsurface geology. This is indicated in figure 3 where the sharp changes in the conductivity and the VSP contours are highly correlated at the water table and at the top of the sand channel. Another area of research that appears ripe for new developments is that of solution appraisal. When we solve an inverse problem, two ingredients are required. First we need to construct a solution and then we need to determine its uncertainty and the ultimate resolving power of the data. In this paper we have primarily considered solution construction. Two recent papers that shed some insight into the appraisal process are those of Alumbaugh and Newman (1999) and Oldenburg and Li (1998). Alumbaugh and Newman utilized linear expansion about the inverse solution to determine the model covariance and model resolution. To treat the nonlinear nature of the problem, Oldenburg and Li propose the use of multiple inversion runs with different starting models to characterize those portions of the solution that are invariant and are well determined by the data. It should be clear that the appraisal process is far more computationally burdensome than construction. It is our contention that to really treat the problem, faster appraisal methods are needed along with more robust techniques to deal with the nonlinear nature of the problem.

Acknowledgments

We thank Dr Michael Wilt, of Electromagnetic Instruments for access to the cross-well data sets and Susan Minkoff and C J Weiss for their critical review of the manuscript. This work was performed at Sandia National Laboratory and Lawrence Berkeley National Laboratory, with funding provided by the United States Department of Energy's Office of Basic Energy Sciences, Division of Engineering and Geoscience. Sandia is a multi-programme laboratory operated by the Sandia Corporation, a Lockheed Martin Company, for the United States Department of Energy under Contract DE-AC04-94AL85000.

References

- Alumbaugh D L and Morrison H F 1995 Theoretical and practical considerations for cross-well electromagnetic tomography assuming a cylindrical geometry *Geophysics* **60** 846–70
- Alumbaugh D L and Newman G A 1999 Image appraisal for 2D and 3D electromagnetic inversion *Geophysics* at press
- 1997 Three-dimensional massively parallel electromagnetic inversion-II. Analysis of a cross-well experiment *Geophys. J. Int.* **128** 355–63
- Alumbaugh D L, Newman G A, Prevost L and Shadid J N 1996 Three-dimensional wide band electromagnetic modelling in massively parallel computers *Radio Sci.* **31** 1–23
- Asher U, Mattheij R and Russell R 1995 *Numerical Solution of Boundary Value Problems for Ordinary Differential Equations* (Philadelphia, PA: SIAM)
- Constable S, Parker R and Constable C 1987 Occam's inversion: A practical algorithm for generating smooth models from electromagnetic sounding data *Geophysics* **52** 289–300
- deGroot-Hedlin C and Constable S C 1990 Occam's inversion to generate smooth, two-dimensional models from magnetotelluric data *Geophysics* **55** 1613–24
- Dennis and Schnabel 1996 *Numerical Methods for Unconstrained Optimization and Nonlinear Equations* (Philadelphia, PA: SIAM)
- Eaton R A 1987 Three-dimensional electromagnetic inversion *PhD Thesis* University of Utah
- Farquharson C G and Oldenburg D W 1996 Approximate sensitivities for the electromagnetic inverse problem *Geophys. J. Int.* **126** 235–52
- Fletcher R and Jackson M P 1974 Minimization of a quadratic function of many variables subject to lower and upper bounds *J. Inst. Math. Appl.* **14** 159–74

- Freund R W and Malhotra M 1995 A block-QMR algorithm for non-Hermitian linear systems with multiple right hand sides *Numerical Analysis Manuscript* No 95-09 (Murray Hill, NJ: AT & T Bell Laboratories)
- Haber E, Ascher U M and Oldenburg D W 1999a A comparison of strategies for solving nonlinear inverse problems *Proc. 14th Ann. Conf. on Multigrid Methods (University of Colorado, Boulder, CO)*
- 1999b Inversion of 3D electromagnetic data *Proc. 2nd Int. Symp. on Three Dimensional Electromagnetics (University of Utah, Salt Lake City, 27–30 October 1999)*
- Heinkenschloss M 1996 Projected sequential quadratic programming methods *SIAM J. Optim.* **6** 373–417
- Hoversten M H, Morrison H F and Constable S C 1998 Part II: Numerical analysis of subsalt resolution *Geophysics* **63** 826–40
- Lin C and Moore J 1999 Newton's method for large bound-constrained optimization problems *SIAM J. Optim.* **9** 1100–27
- Mackie R L and Madden T R 1993 Three-dimensional magnetotelluric modelling and inversion using conjugate gradients *Geophys. J. Int.* **115** 215–29
- Newman G A 1999 Three-dimensional magnetotelluric modelling and inversion *Proc. 2nd Int. Symp. on Three Dimensional Electromagnetics (University of Utah, Salt Lake City, 27–30 October 1999)*
- 1995 Cross-well electromagnetic inversion using integral and differential equations *Geophysics* **60** 899–911
- Newman G A and Alumbaugh D L 1999 Electromagnetic modelling and inversion on massively parallel computers *Three Dimensional Electromagnetics* (Tulsa, OK: Society of Exploration Geophysicists) pp 299–321
- 1997 Three-dimensional massively parallel electromagnetic inversion-I. Theory *Geophys. J. Int.* **128** 345–54
- 1996 Electromagnetic modelling of subsurface 3D structures *IGARSS: Proc. Int. Geoscience and Remote Sensing Symposium (Omaha, Nebraska)* pp 1941–4
- 1995 Frequency-domain modelling of airborne electromagnetic responses using staggered finite differences *Geophys. Prospect.* **43** 1021–42
- Oldenburg D W and Li Y 1998 Estimating the depth of investigation in DC resistivity and IP surveys *Geophysics* **64** 403–16
- Scales J A, Docherty P and Gersztenkorn A 1990 Regularization of nonlinear inverse problems: imaging the near-surface weathering layer *Inverse Problems* **6** 115–31
- Smith T, Hoversten M, Gasperikova E and Morrison F 1999 Sharp boundary inversion of 2D magnetotelluric data *Geophys. Prospect.* **47** 469–86
- Smith J T 1996a Conservative modelling of 3D electromagnetic fields; Part I: Properties and error analysis *Geophysics* **61** 1308–18
- 1996b Conservative modelling of 3D electromagnetic fields; Part II: Biconjugate gradient solution and an accelerator *Geophysics* **61** 1319–24
- Stoyer C H and Greenfield R J 1976 Numerical solutions of the response of a two-dimensional earth to an oscillating magnetic dipole source *Geophysics* **41** 519–30
- Tikhonov A N and Arsenin V Y 1977 *Solutions to Ill-Posed Problems* (New York: Wiley)
- Torres-Verdin C and Habashy T M 1994 Rapid 2.5-dimensional forward modelling and inversion via a new nonlinear scattering approximation *Radio Sci.* **29** 1051–79
- Wilt M L, Schenkel C, Spies B, Torres-Verdin C and Alumbaugh D L 1999 Measurements of surface and borehole electromagnetic fields in 2D and 3D geology *Three Dimensional Electromagnetics* (Tulsa, OK: Society of Exploration Geophysicists) pp 545–63
- Yee K S 1966 Numerical solution of initial boundary problems involving Maxwell equations in isotropic media *IEEE Trans. Antennas Propag.* **14** 302–9
- Zhdanov M S and Fang S 1999 3D electromagnetic inversion based on the quasi-linear approximation *Three Dimensional Electromagnetics* (Tulsa, OK: Society of Exploration Geophysicists) pp 233–55